

Investigation of reflection anisotropy induced by micropipe defects on the surface of a 4H-SiC single crystal using scanning anisotropy microscopy

Wei Huang(黄威), Jinling Yu(俞金玲), Yu Liu(刘雨), Yan Peng(彭燕), LiJun Wang(王利军), Ping Liang(梁平), Tangsheng Chen(陈堂胜), Xiangang Xu(徐现刚), Fengqi Liu(刘峰奇), and Yonghai Chen(陈涌海)
Citation: Chin. Phys. B, 2024, 33 (**3**): 037801. DOI: 10.1088/1674-1056/acf27f
Journal homepage: http://cpb.iphy.ac.cn; http://iopscience.iop.org/cpb

What follows is a list of articles you may be interested in

Ultrafast magneto-optical dynamics in nickel (111) single crystal studied by the integration of ultrafast reflectivity and polarimetry probes

Hao Kuang(匡皓), Junxiao Yu(余军潇), Jie Chen(陈洁), H. E. Elsayed-Ali, Runze Li(李润泽), and Peter M. Rentzepis
Chin. Phys. B, 2024, 33 (**3**): 037802. DOI: 10.1088/1674-1056/ad1983

Shape and diffusion instabilities of two non-spherical gas bubbles under ultrasonic conditions

Wurihan Bao(包乌日汗) and De-Xin Wang(王德鑫)
Chin. Phys. B, 2024, 33 (**1**): 017803. DOI: 10.1088/1674-1056/acfa81

Optical study of magnetic topological insulator $MnBi_4Te_7$

Zhi-Yu Liao(廖知裕), Bing Shen(沈冰), Xiang-Gang Qiu(邱祥冈), and Bing Xu(许兵)
Chin. Phys. B, 2024, 33 (**1**): 017802. DOI: 10.1088/1674-1056/ad08aa

Valley transport in Kekulé structures of graphene

Juan-Juan Wang(王娟娟) and Jun Wang(汪军)
Chin. Phys. B, 2024, 33 (**1**): 017801. DOI: 10.1088/1674-1056/acf9e3

Elemental composition x-ray fluorescence analysis with a TES-based high-resolution x-ray spectrometer

Bingjun Wu(吴秉骏), Jingkai Xia(夏经铠), Shuo Zhang(张硕), Qiang Fu(傅强), Hui Zhang(章辉),Xiaoming Xie(谢晓明), and Zhi Liu(刘志)
Chin. Phys. B, 2023, 32 (**9**): 097801. DOI: 10.1088/1674-1056/acd926

Investigation of reflection anisotropy induced by micropipe defects on the surface of a 4H-SiC single crystal using scanning anisotropy microscopy

Wei Huang(黄威)[1,2,3,†], Jinling Yu(俞金玲)[4,†], Yu Liu(刘雨)[1,‡], Yan Peng(彭燕)[5], Lijun Wang(王利军)[1], Ping Liang(梁平)[1], Tangsheng Chen(陈堂胜)[3], Xiangang Xu(徐现刚)[5], Fengqi Liu(刘峰奇)[1], and Yonghai Chen(陈涌海)[1,2,§]

[1] *Key Laboratory of Semiconductor Materials Science, Institute of Semiconductors, Chinese Academy of Sciences, Beijing* 100083, *China*
[2] *College of Materials Science and Opto-Electronic Technology, University of Chinese Academy of Sciences, Beijing* 100049, *China*
[3] *National Key Laboratory of Solid-state Microwave Devices and Circuits, Nanjing Electronic Devices Institute, Nanjing* 210016, *China*
[4] *Institute of Micro/Nano Devices and Solar Cells, School of Physics and Information Engineering, Fuzhou University, Fuzhou* 350108, *China*
[5] *State Key Laboratory of Crystal Materials, Shandong University, Jinan* 250100, *China*

(Received 15 June 2023; revised manuscript received 6 August 2023; accepted manuscript online 22 August 2023)

Optical reflection anisotropy microscopy mappings of micropipe defects on the surface of a 4H-SiC single crystal are studied by the scanning anisotropy microscopy (SAM) system. The reflection anisotropy (RA) image with a 'butterfly pattern' is obtained around the micropipes by SAM. The RA image of the edge dislocations is theoretically simulated based on dislocation theory and the photoelastic principle. By comparing with the Raman spectrum, it is verified that the micropipes consist of edge dislocations. The different patterns of the RA images are due to the different orientations of the Burgers vectors. Besides, the strain distribution of the micropipes is also deduced. One can identify the dislocation type, the direction of the Burgers vector and the optical anisotropy from the RA image by using SAM. Therefore, SAM is an ideal tool to measure the optical anisotropy induced by the strain field around a defect.

Keywords: scanning anisotropy microscopy, SiC, reflection anisotropy, edge dislocation

PACS: 78.20.H–, 78.20.Ci, 33.20.Fb, 68.35.Gy **DOI:** 10.1088/1674-1056/acf27f

1. Introduction

A silicon carbide (SiC) single crystal is a typical representative of the third generation of wide band gap semiconductor material with the advantages of large band gap, high breakdown field, high thermal conductivity, high electron saturation velocity, high temperature stability and low dielectric losses.[1–5] The outstanding physical properties of SiC make it suitable for producing high-temperature, high-frequency and high-power devices, and it is becoming a new strategic focus of the global semiconductor industry.[6–8] In the past few decades, much effort has been devoted to achieving large-size, high-quality single crystals of SiC. As crystal growth techniques have developed rapidly, the density of microstructural defects has been reduced greatly. However, it is still an arduous task to completely eliminate them (especially dislocations, micropipes, etc) in SiC single crystals. Moreover, microstructural defects in the semiconductor material directly affect the quality of epitaxial material and the performance of devices, especially high-power devices.[9–12]

In addition to solving the problems of reducing or eliminating microstructural defects such as dislocations and micropipes, it is more important to have a thorough understanding of their formation mechanism. The formation mechanism of micropipes is widely recognized by Frank's theory,[13] which interprets this formation mechanism as the stress relaxation of screw dislocations with large Burgers vectors. Recently, Ning *et al.* proposed a hypothesis based on the fact that micropipes are pure screw dislocations to explain the stress birefringence imaging of micropipes.[9] However, Presser, Vetter and Ouisse have demonstrated that the micropipes contain not only screw dislocations with large Burgers vectors but also edge dislocation components by using conventional polarizing microscopy, transmission electron microscopy (TEM) and high-resolution x-ray diffraction (XRD).[14–17] Therefore, controversies still exist over the formation mechanism of micropipes, and it is of great significance to develop a suitable and nondestructive evaluation technique that can fully characterize the micropipe defects and study their formation mechanism, thus providing guidance for the growth of materials. Compared with the methods used in the previous works reported in Refs. [14–17], the method used in this work can obtain information on the microstructural defects by measuring optical anisotropy around them, and it has the advantages of high accuracy, high sensitivity and being non-destructive.

In this paper, we have used scanning anisotropy microscope (SAM) and the micro-Raman technique to characterize the micropipe and investigate its formation mechanism,

[†]These authors contributed equally to this work.
[‡]Corresponding author. E-mail: liuyu@semi.ac.cn
[§]Corresponding author. E-mail: yhchen@semi.ac.cn

© 2024 Chinese Physical Society and IOP Publishing Ltd

by studying the optical anisotropy of the micropipe on the surface of 4H-SiC single crystals. The reflection anisotropy (RA) image with a 'butterfly pattern' is obtained around the micropipes by SAM. Combining with the micro-Raman technique and theoretical calculations, it is demonstrated that the micropipes consist of edge dislocations.

2. Sample preparation and methods

2.1. Sample preparation

The 4H-SiC single crystal was grown by the sublimation method.[18] The SiC source powder was placed on the bottom of a graphite crucible, and the seed crystal was mounted on the top of the crucible. The SiC source powder was sublimated by heating with an RF generator at a frequency of 10 kHz. The crucible lid was covered with a graphite foil so that it could be used repeatedly. During the crystal growth, the temperature of the crucible lid was kept at 2100 °C and the temperature gradient was 50 °C·cm^{-1}. In the growth chamber, argon was used as the carrier gas and the chamber pressure was kept at 100–800 mbar. The growth of the 4H-SiC single crystal was terminated after 40 hours and it was cooled to room temperature. Then, 4H-SiC wafers were obtained by cutting, grinding and polishing the native SiC crystals; the thickness of each wafer was about 400 μm. The surface of a wafer is parallel to the (0001) plane and the polished surface is the Si-polar plane.

Owing to the specific structure of SiC, hollow tubes called micropipes are often found in the sublimation-grown SiC crystal. Micropipes with a size of 0.1–5 μm generally run along the c axis, and they are fatal for device applications.[9] To observe a high density of micropipe defects, we chose to investigate SiC wafers with defect densities ranging from 5 cm^{-2} to 50 cm^{-2}. A series of metal markers have been placed on the 4H-SiC surface by photolithography and vapor deposition, and they help us find the same measurement area after the rotation of the sample. The sample is ultrasonically cleaned before each measurement.

2.2. Experiments

SAM can measure optical anisotropy images around these microstructural defects based on the photoelasticity effect.[19,20] A schematic diagram of the SAM system is shown in Fig. 1, and it is the same as that used in Ref. [21]. In the SAM system, two lock-in amplifiers are used in the signal detection system to obtain the normal reflectivity (R) signals and the reflection anisotropy (RA) signals of the 4H-SiC. A solid-state laser with a wavelength of 532 nm and power of 300 mW is used as the light source. After passing through a spatial filter, the laser beam goes through a polarizer and a photoelastic modulator (PEM). Then the beam is split by a polarization-preserving 50/50 beam splitter into an objective lens of long working distance (Mitutoyo 100X, numerical aperture = 0.55), and is focused on the sample placed on a piezoelectric ceramic electric translation stage, which can move in two dimensions in a plane. The reflected beam, after passing through the objective lens and the beam splitter, is directed to an analyzer and then focused onto a silicon detector.

The reason why the SAM system is capable of capturing RA images around the micropipe defects is that the micropipe will introduce strain around the micropipe, which will lead to reflection anisotropy around the micropipe. In the SAM system, a PEM together with a polarizer will make the polarization state of the light change periodically between linearly polarized light polarized in the x direction and polarized in the y direction. By using an analyzer placed after the sample and a lock-in amplifier, we can detect the reflection anisotropy in the x and y directions around the micropipe. Here x and y are the two in-plane orthogonal directions.

The R signal is the intensity signal of reflectivity, which is detected by a lock-in amplifier referenced by a chopper of 220 Hz. The RA signal is the optical anisotropy signal detected by a lock-in amplifier referenced by a PEM of base frequency $\omega = 50$ kHz. By changing the position of the light spot on the sample and recording the signal at each position, we can obtain the R mapping and RA mapping of the 4H-SiC.

Raman mapping was also performed in the backscattering configuration at room temperature using a Jobin–Yvon HR Evolution micro-Raman system, equipped with a liquid-nitrogen-cooled charge-coupled detector camera. The excitation light is from a diode-pumped solid-state laser with a wavelength of 532 nm. Passing through a ×100 microscope objective (numerical aperture = 0.90), the light is focused on the sample with a diameter of approximately 1 μm and a power of 10 mW. The spectral resolution of the Raman spectrometer is 0.35 cm^{-1}.

2.3. Theory

The SAM system can precisely measure the in-plane optical anisotropy (IPOA) by measuring the relative difference in reflection coefficient between the two in-plane orthogonal directions, denoted as x and y, which is defined as[22–25]

$$\frac{\Delta r}{r} = \frac{2(r_x - r_y)}{r_x + r_y}. \tag{1}$$

Here r_x and r_y are the reflection coefficients in the x and y directions, respectively. r is the averaged reflection coefficient, i.e., $r = (r_x + r_y)/2$, and $\Delta r = r_x - r_y$. The intensity of the reflected light arriving at the detector can be expressed as

$$I = \frac{RE_0^2}{2}\left[1 + J_0(\phi)\mathrm{Re}\left(\frac{\Delta r}{r}\right) + 2J_1(\phi)\mathrm{Im}\left(\frac{\Delta r}{r}\right)\sin\omega t + 2J_2(\phi)\mathrm{Re}\left(\frac{\Delta r}{r}\right)\cos 2\omega t\right]. \tag{2}$$

Here $R = |r_x + r_y|^2/4$ is the reflectivity of the sample, and E_0^2 represents the intensity of the reflected light. ϕ is the phase retardation induced by the PEM. J_0, J_1 and J_2 are Bessel functions, and ω is the base modulation frequency of the PEM.

$\mathrm{Re}(\Delta r/r)$ and $\mathrm{Im}(\Delta r/r)$ are the real and imaginary components of $\Delta r/r$, respectively. By adopting ϕ to be 0.383λ, we have $J_0 = 0$. Thus, the R signal of the system is proportional to the intensity of the light recorded by the detector. Since the RA signal varies at a frequency of ω, its intensity is proportional to the imaginary part of $\Delta r/r$, reflecting the IPOA of the sample.

Given that $r = \sqrt{R}\exp(\mathrm{i}\phi)$, equation (1) can also be written as

$$\frac{\Delta r}{r} = \frac{1}{2}\frac{\Delta R}{R} + \mathrm{i}\Delta\varphi. \tag{3}$$

Comparing Eq. (3) with Eq. (2), we find that the RA signal is essentially the phase difference between the light polarized in the x direction and that in the y direction of the detected light, i.e., $\Delta\varphi$.

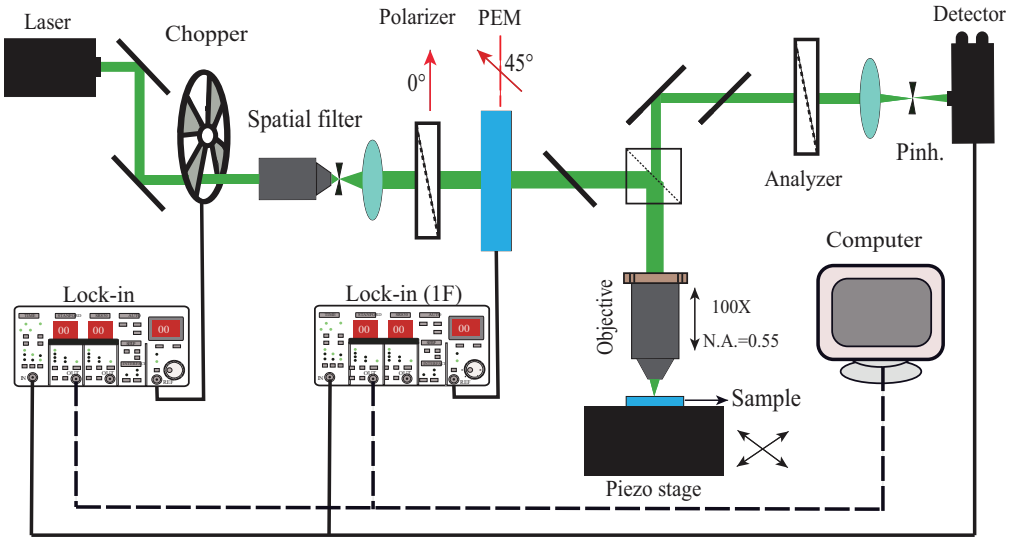


Fig. 1. Schematic diagram of the SAM system.

3. Results and discussion

3.1. RA images of the SiC micropipe defects

Figure 2 shows the R and RA images of the two micropipes obtained by the SAM system. Figures 2(a) and 2(c) are the R images of the micropipes M1 and M2, respectively. The R image represents the surface topography of the sample,[21] and the blue spot in the middle of the R image indicates the micropipe. The small green spots near the micropipes in the R image have been confirmed to be dust on the surface of the sample. Figures 2(b) and 2(d) are the RA images of M1

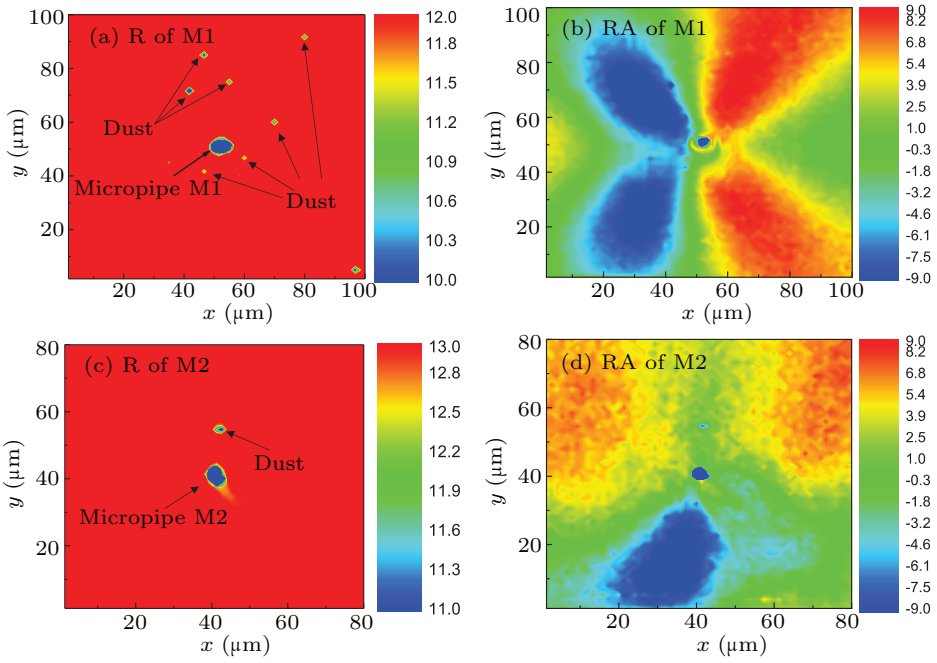


Fig. 2. Two typical SAM images of micropipes. (a) and (b) The normal R and RA images of micropipe M1, respectively. (c) and (d) The R and RA images of micropipe M2, respectively. The signal unit in (a) and (c) is 1, and that in (b) and (d) is 10^{-3}.

and M2, respectively. The RA image of M1 exhibits a butterfly-like pattern with four bright wings (one pair shows positive values, and the other pair negative). The RA image of M2 is similar to that of M1 except that the orientation of the butterfly-like pattern is different. From the discussion below, it can be seen that this is due to the different orientations of the Burgers vectors.

3.2. Discussion and analysis of the RA image

3.2.1. Theoretical analysis of the RA image

It has been found that RA images are reflection optical anisotropy signals ($\Delta\varphi$) generated at the interface between two different materials, or induced by the height of the step on the nanometer scale, or due to linear defects on the surface of the material.[19,26–28] The RA image of the micropipe may be caused by the strain field around it. The relation between the reflection optical anisotropy signal $\Delta\varphi$ and the strain tensor ε can be expressed as[29]

$$\Delta\varphi \propto \frac{1}{2} f(\varepsilon_{xx}, \varepsilon_{yy}, \varepsilon_{xy}). \tag{4}$$

Here $\Delta\varphi$ is the phase difference, which represents the relative difference in reflection coefficient in two perpendicular in-plane directions for each test point. ε_{xx}, ε_{yy} and ε_{xy} are the components of strain tensors. f in Eq. (4) is a complex function, from which we can calculate the RA image, related to the strain field.

Although there are still controversies, it is quite certain that micropipes are related to dislocations. Therefore, it is necessary to theoretically analyze the RA image induced by dislocations. Dislocations include edge dislocations and screw dislocations. For edge dislocations, $\varepsilon_{xx} \neq 0$, $\varepsilon_{yy} \neq 0$, $\varepsilon_{zz} \neq 0$, $\varepsilon_{xy} \neq 0$, and the other components are zero, i.e., the stress tensor induced by the edge dislocation can be expressed as

$$\begin{vmatrix} \varepsilon_{xx} & \varepsilon_{xy} & 0 \\ \varepsilon_{yx} & \varepsilon_{yy} & 0 \\ 0 & 0 & \varepsilon_{zz} \end{vmatrix}. \tag{5}$$

Obviously, the z axis is one of the principal axes. Since the SAM system only measures the optical anisotropy in the x–y plane, it is not necessary to take into account the stress component in the z direction, i.e., ε_{zz}. The eigenequations of the in-plane strain field can be expressed as

$$\begin{pmatrix} \varepsilon_{xx} & \varepsilon_{xy} \\ \varepsilon_{xy} & \varepsilon_{yy} \end{pmatrix} \begin{bmatrix} e_x \\ e_y \end{bmatrix} = \varepsilon \begin{bmatrix} e_x \\ e_y \end{bmatrix}. \tag{6}$$

From Eq. (6) we can obtain the eigenvalue of the stress in the x–y plane, which can be written as

$$\varepsilon = \frac{(\varepsilon_{xx} + \varepsilon_{yy}) \pm \sqrt{(\varepsilon_{xx} - \varepsilon_{yy})^2 + 4\varepsilon_{xy}^2}}{2}, \tag{7}$$

and the corresponding eigenvectors are

$$\begin{pmatrix} e_x \\ e_y \end{pmatrix} = \begin{pmatrix} 1 \\ \frac{2\varepsilon_{xy}}{(\varepsilon_{xx} - \varepsilon_{yy}) + \sqrt{(\varepsilon_{xx} - \varepsilon_{yy})^2 + 4\varepsilon_{xy}^2}} \end{pmatrix}. \tag{8}$$

The difference between the two stress eigenvalues is

$$\Delta\varepsilon = \sqrt{(\varepsilon_{xx} - \varepsilon_{yy})^2 + 4\varepsilon_{xy}^2}. \tag{9}$$

When $\varepsilon_{xy} = 0$, the principal axis of strain is in the x direction. When $\varepsilon_{xy} \neq 0$, the principal axis of strain will rotate by an angle of θ_0 with respect to the x axis, and the angle θ_0 can be expressed as

$$\tan\theta_0 = \frac{2\varepsilon_{xy}}{(\varepsilon_{xx} - \varepsilon_{yy}) + \sqrt{(\varepsilon_{xx} - \varepsilon_{yy})^2 + 4\varepsilon_{xy}^2}}. \tag{10}$$

At the spatial position (x, y), the maximum optical anisotropy is proportional to $\Delta\varepsilon$. Therefore, the IPOA of the point (x, y) can be expressed as

$$I_{\mathrm{RA}} = (I_{\mathrm{RA}})_{\max} \times \cos 2\theta_0 \propto \sqrt{(\varepsilon_{xx} - \varepsilon_{yy})^2 + 4\varepsilon_{xy}^2} \cos 2\theta_0. \tag{11}$$

Thus, for edge dislocations, the IPOA at the point (x, y) induced by the strain field of the edge dislocations is

$$I_{\mathrm{RA}} \propto \sqrt{(\varepsilon_{xx} - \varepsilon_{yy})^2 + 4\varepsilon_{xy}^2} \cos 2(\theta_0 + \varphi). \tag{12}$$

Here φ is the angle between Burgers vector and the x axis.

According to the elastic theory, the strain components of the edge dislocations can be expressed in polar coordinates as

$$\begin{cases} \sigma_{rr} = \sigma_{\vartheta\vartheta} = -D\dfrac{\sin\vartheta}{r}, \\ \sigma_{r\vartheta} = D\dfrac{\cos\vartheta}{r}, \\ \sigma_{zz} = -2D\upsilon\dfrac{\sin\vartheta}{r}. \end{cases} \tag{13}$$

Here $D = -\frac{\mu b}{2\pi(1-\upsilon)}$, with μ being the shear modulus, υ being Poisson's ratio and b being the Burgers vector. According to Eq. (13), we can obtain the following equations through the transformation relation between the strain tensor and stress tensor:

$$\begin{cases} \varepsilon_{xx} - \varepsilon_{yy} = 2D(1 + \cos 2\vartheta) \times \dfrac{\sin\vartheta}{r}, \\ \varepsilon_{xy} = D\cos 2\vartheta \times \dfrac{\sin\vartheta}{r}. \end{cases} \tag{14}$$

By substituting the stress tensor of the edge dislocations into Eqs. (10) and (12), we can calculate the RA images with Burgers vectors directed in different directions theoretically, as shown in Fig. 3.

The strain field of screw dislocations is much simpler than that of edge dislocations. According to the dislocation theory in reference,[30] the strain component of the screw dislocation can be expressed in polar coordinates as

$$\sigma_{\vartheta z} = \frac{\mu b}{2\pi r}, \tag{15}$$

where μ is the shear modulus and b is the Burgers vector. Here the center of the screw dislocation is set as the origin of the coordinates, and r is the distance from the origin. The remaining components are all zero, i.e., $\sigma_{rr} = \sigma_{r\vartheta} = \sigma_{rz} = 0$. It can be seen from Eq. (15) that the shear stress component produced by the screw dislocation is inversely proportional to r, and the stress field of the screw dislocation is axisymmetric. Through the conversion relationship between the strain tensor and the stress tensor, it is obvious that the strain components of the screw dislocation in the x and y directions are zero. Therefore, the stress field of the screw dislocation does not cause the IPOA signal between the x and y directions ($\Delta\varphi = 0$).

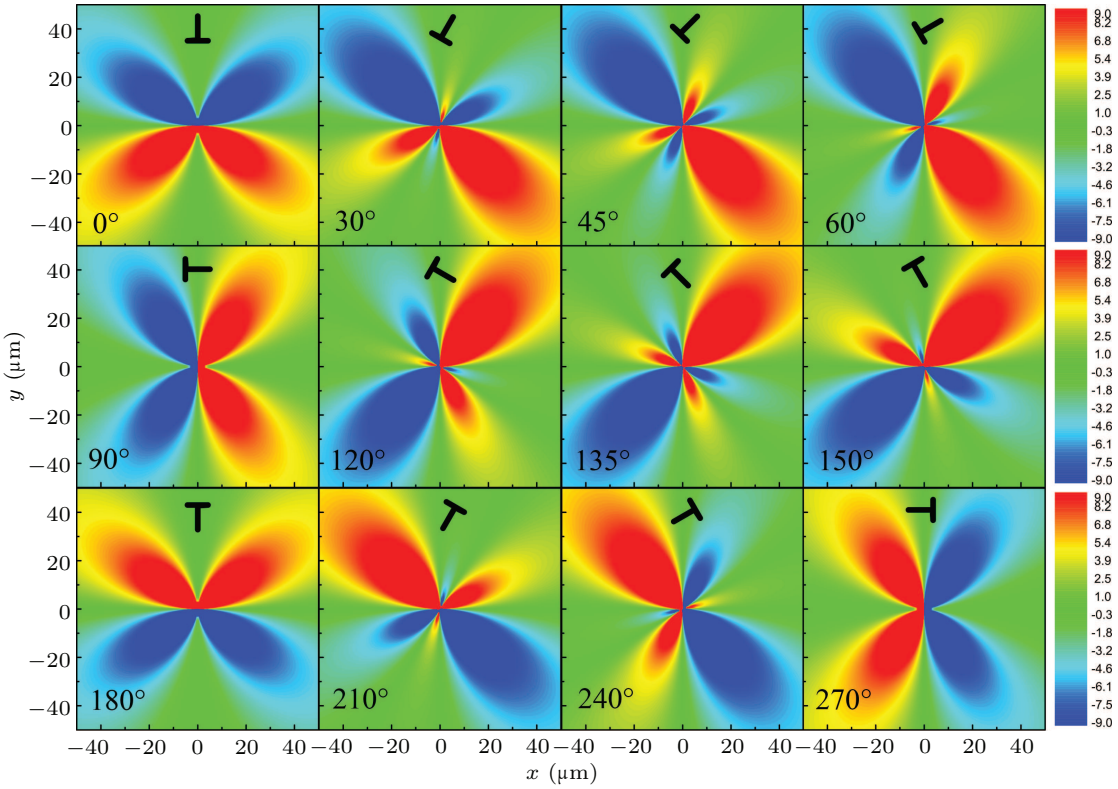


Fig. 3. Simulated RA image of the edge dislocations with Burgers vectors in different directions. '⊥' indicates the direction of the Burgers vector.

3.2.2. Discussion and analysis of the RA image of M1

It can be seen from Fig. 2(b) that the RA image shows a typical butterfly-like shape, which is essentially the same as the butterfly-like stress birefringence imaging obtained by the polarization microscope,[9,16] except that the RA image shows a polar distribution. Based on the theory of the photoelastic effect, the RA image is generated by in-plane stress ε_{xx} and $\varepsilon_{xx} - \varepsilon_{yy}$. According to the above theoretical analysis of the screw dislocation, it is known that the screw dislocation does not generate an RA signal in the x–y plane ($\Delta\varphi = 0$). For the edge dislocations, the non-zero stress components are ε_{xx}, ε_{yy}, ε_{zz} and ε_{xy}, i.e., ε_{xy} and $\varepsilon_{xx} - \varepsilon_{yy}$ are not zero, leading to an RA signal in the x–y plane ($\Delta\varphi \neq 0$).[31,32] Therefore, the edge dislocation component must be taken into account in the analysis of the RA signal of the micropipes.

To obtain knowledge of the strain distribution around the micropipes, we performed micro-Raman measurements, since the Raman frequency shift of the modes E_1(TO) and E_2(TO) reflects the strain state of the sample. Figure 4(a) shows the Raman spectrum of the 4H-SiC in a region without micropipes. The peaks of E_2(TO), E_1(TO) and A_1(LO) are located at about 776.5 cm^{-1}, 797.3 cm^{-1} and 965.1 cm^{-1}, respectively, which are consistent with other reports.[33,34] Figure 4(b) shows the peak position mapping of E_2(TO) around the M1, and Fig. 4(c) shows the mapping of the peak positions of E_1(TO) around M1. They all exhibit a dipole-moment-like distribution. Obviously, the peak position of E_2(TO) is more sensitive to strain than that of E_1(TO), which indicates that the E_2(TO) mapping is more accurate for characterizing the strain field.

In Fig. 4(b), the redshift or blueshift of the E_2(TO) mode is within the range $\pm$0.6 cm^{-1}. A compressive strain in the film will reduce the bond lengths and the vibration frequency of atoms, leading to a blueshift of Raman peaks; conversely, a tensile strain will lead to a redshift. Therefore, the red lobe (blueshift) in Fig. 4(b) indicates that the area of the film is under compressive strain, while the blue lobe (redshift) suggests that it is under tensile strain. This energy shift is due to elastic lattice deformation by the strain field of the edge dislocation,[35] i.e., on one side of the dislocation the additional lattice plane causes compressive strain, whereas on the opposite side a tensile strain is induced. The strain field distribution indicates that the dislocation is an edge dislocation,

and the Burgers vector is directed along the x axis, as denoted by the '⊢' in Fig. 4.

Figure 4(d) shows the simulation result of the RA image based on an ideal edge dislocation with the Burger vector directed along the x axis. Comparing Fig. 4(d) with Fig. 2(b), one can see that the simulation result shows the same shape as that observed in the experiment, which suggests that the simulation result agrees very well with experimental results. The simulation result confirms our inference about the nature of the micropipes, i.e., that they are edge dislocations.

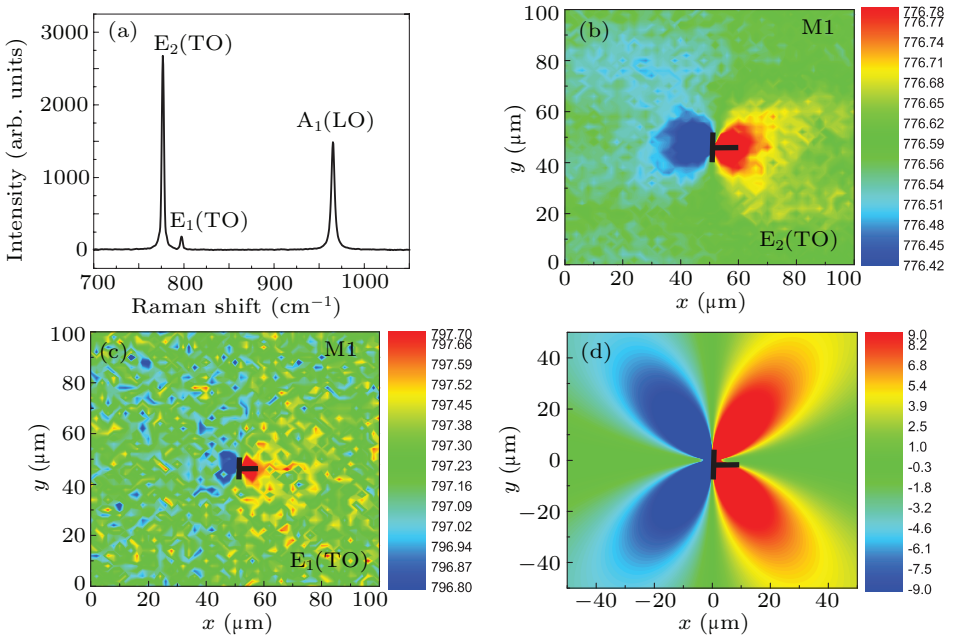


Fig. 4. Raman spectra and the simulated RA image around the micropipe M1. (a) Raman spectrum of the 4H-SiC wafer in a region without micropipes. (b) The Raman peak position mapping of E_2(TO) mode around the micropipe M1. (c) Raman peak position mapping of E_1(TO) mode around the micropipe M1 for an azimuth angle θ of 0°. (d) The simulated RA image around the micropipe M1 when the Burgers vector is in the x direction, which is indicated by the symbol '⊢'.

3.2.3. Discussion and analysis of the RA image of M2

Interestingly, the RA image of the micropipe M2 shows different distributions in direction to that of M1. To find out the reason, we measure the Raman mapping of the E_2(TO) mode of the micropipe M2, and the result is shown in Fig. 5(a). It can be seen from Fig. 5(a) that the 'dipole' of M2 shows a 60° rotation compared with that of M1, which indicates that the Burgers vector in M2 is rotated by an angle of 60°, according to the above analysis of the Raman mapping and the RA image. Different orientations of the Burgers vector will lead to the different strain components that show up in the RA images, thus resulting in different RA images.

Figures 5(b) and 5(c) show the stress birefringence images around the micropipe M2 at azimuth angles θ of 0° and 90°, respectively, obtained by the polarization microscope. It can be seen that the polarization microscope also shows different shapes as the sample rotates, but the sign remains the same. This is because the stress birefringence signal obtained by the polarization microscope is proportional to the absolute value of the IPOA. The RA images obtained from the SAM system and the stress birefringence images obtained through polarized microscopy show the same patterns, and both of them change with the orientation of the Burgers vectors. The differences between them are that the RA images exhibit positive and negative values, which makes it easy to distinguish the orientation of the edge dislocations, while the stress birefringence images obtained by polarized microscopy show the same sign, and it is difficult to determine the orientation of the edge dislocations.

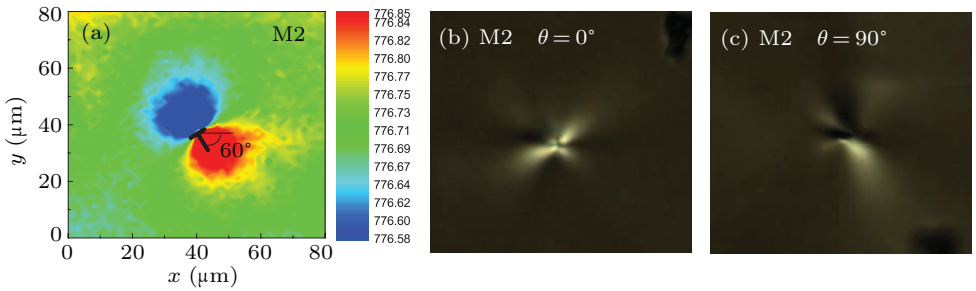


Fig. 5. (a) Raman peak position mapping of the E_2(TO) mode around the micropipe M2. The azimuth angle θ adopted here is the same as that adopted in Fig. 2. (b), (c) Stress birefringence images around the micropipe M2 at azimuth angles θ of 0° and 90°, respectively, obtained by the polarization microscope.

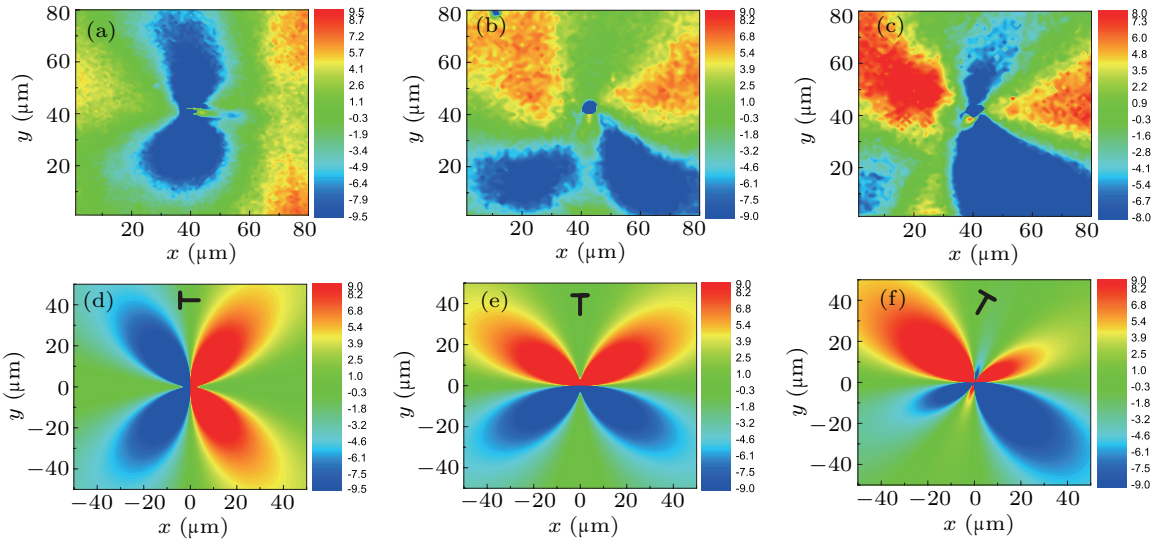


Fig. 6. Experimental and simulated results of the RA images around the micropipe M2 for different azimuth angles θ. (a)–(c) Experimental results of the RA images at θ of 0°, 90° and 120°, respectively. (d)–(f) Simulated results of the RA images at θ of 0°, 90° and 120°, respectively.

To further confirm our model, we measure the RA images of the micropipe M2 for different orientations of Burgers vectors, which is achieved by rotating the sample in the x–y plane around the axis that goes through the micropipe. Specifically, we rotate the sample 60° anticlockwise firstly. Thus, the Burgers vector of M2 is directed along the x axis, which is the same as that of M1. Denoting this azimuth angle as 0°, i.e., $\theta = 0°$, we measure the RA image of M2 for this azimuth angle, as shown in Fig. 6(a). Then, after rotating the sample 90° and 120° clockwise, respectively, i.e., $\theta = 90°$ and 120°, we measure the RA images correspondingly, and the results are shown in Figs. 6(b) and 6(c), respectively.

It can be seen from Fig. 6 that the experimental results are essentially in agreement with the theoretical calculation, because they show a similar pattern. The slight difference between experimental data and the theoretical results may be due to the fact that the micropipe is not strictly perpendicular to the surface of the sample, but we do not take this effect into account. Comparing the experimental and theoretical results, we can come to the following conclusions. Firstly, the differences between the RA images of M1 and M2 shown in Figs. 2(b) and 2(d), respectively, are caused by the different orientations of the Burgers vectors. When the Burgers vector of M2 is rotated to align in the same direction as that of M1, their RA images show the same shape, which is induced by the IPOA of the strain field due to the edge dislocations. Secondly, only when the Burgers vector is directed along the x or y axis can the RA image present a butterfly-like shape. Thirdly, the sign of the RA image for a certain area is reversed when the sample is rotated 90°, which is consistent with the observations reported in previous studies.[21,29]

From the above analysis, one can see that the distinct features and characteristics of the RA images for micropipes are that the RA images show a butterfly-like pattern with some 'wings' positive and other 'wings' negative. In essence, micropipes are actually dislocations. Combining with the theoretical calculation, we have demonstrated that the butterfly-like RA image is due to the edge dislocation. The shape of the butterfly-like pattern is related to the orientation of the Burgers vectors. By rotating the sample, the RA image will show different patterns.

4. Conclusion

In conclusion, we have investigated the optical reflection anisotropy microscopy mappings of micropipe defects on the surface of a 4H-SiC single crystal by using the SAM system. The RA image with a 'butterfly pattern' is obtained around the micropipes with this system. By comparing the experimental results of the RA images with the Raman mapping, we find that the micropipes consist of edge dislocations with relatively large Burgers vectors. Besides, the strain distribution around the micropipes is also deduced. It is revealed that the RA image obtained by SAM shows the same shape as the stress birefringence image obtained by a polarization microscope, but the RA image can distinguish positive and negative stresses. Besides, the resolution of SAM is higher than that of the micro-Raman technique and a polarization microscope. This work further suggests that SAM is a non-destructive, convenient and effective method for studying the microstructural defects on semiconductor material and device surfaces.

Acknowledgements

Project supported by the National Key Research and Development Program of China (Grant Nos. 2018YFE0204001, 2018YFA0209103, 2016YFB0400101, and 2016YFB0402303), the National Natural Science Foundation of China (Grant Nos. 61627822, 61704121, 61991430, and 62074036), and

Postdoctoral Research Program of Jiangsu Province (Grant No. 2021K599C).

References

[1] Baierhofer D, Thomas B, Staiger F, Marchetti B, Foerster C and Erlbacher T 2022 *Materials Science in Semiconductor Processing* **140** 106414

[2] Wang H, Yu J, Hu G, Peng Y, Xie X, Hu X, Chen X and Xu X 2021 *Materials* **14** 5890

[3] Augustine G, Balakrishna V and Brandt C 2000 *J. Cryst. Growth* **211** 339

[4] Cooper J A 1997 *Physica Status Solidi a-Applied Research* **162** 305

[5] Jenny J, Skowronski M, Mitchel W, Hobgood H, Glass R, Augustine G and Hopkins R 1995 *J. Appl. Phys.* **78** 3839

[6] Siergiej R, Clarke R, Sriram S, Agarwal A, Bojko R, Morse A, Balakrishna V, MacMillan M, Burk A and Brandt C 1999 *Mat. Sci. Eng. B-Solid* **61** 9

[7] Zolper J 2005 *Emerging silicon carbide power electronics components APEC 2005: Twentieth Annual IEEE Applied Power Electronics Conference and Exposition, VOLS 1-3 Annual IEEE Applied Power Electronics Conference and Exposition (APEC)* (IEEE; Power Sources Manufacturers Assoc; IEEE PELS; IEEE Ind Applicat Soc) pp. 11–17

[8] Bhatnagar M, Mclarty P and Baliga B 1992 *IEEE Electron Device Lett.* **13** 501

[9] Ning L, Hu X, Xu X, Chen X, Wang Y, Jiang S and Li J 2008 *Journal of Applied Crystallography* **41** 939

[10] Dadgar A, Hums C, Diez A, Blaesing J and Krost A 2006 *J. Cryst. Growth* **297** 279

[11] Wu Y F, Saxler A, Moore M, Smith R P, Sheppard S, Chavarkar PM, Wisleder T, Mishra U K and Parikh P 2004 *IEEE Electron Device Letters* **25** 117

[12] Wang X and Yoshikawa A 2004 *Molecular beam epitaxy growth of GaN, AlN and InN Progress in Crystal Growth and Characterization of Materials* Vol. 48–49 pp. 42–103

[13] Frank F C 1951 *Acta Crystallographica* **4** 497

[14] Presser V, Loges A and Nickel K G 2008 *Philosophical Magazine* **88** 1639

[15] Vetter WM and Dudley M 2006 *Philosophical Magazine* **86** 1209

[16] Ouisse T, Chaussende D and Auvray L 2010 *Journal of Applied Crystallography* **43** 122

[17] Le Thi Mai H, Ouisse T and Chaussende D 2012 *J. Cryst. Growth* **354** 202

[18] Hu X, Xu X, Li X, Jiang S, Li J, Wang L, Wang J and Jiang M 2006 *J. Cryst. Growth* **292** 192

[19] Koopmans B, Santos P V and Cardona M 1998 *Physica Status Solidi a-Applied Research* **170** 307

[20] Koopmans B, Richards B, Santos P, Eberl K and Cardona M 1996 *Appl. Phys. Lett.* **69** 782

[21] Huang W, Liu Y, Zhu L, Zheng X, Li Y, Wu Q, Wang Y, Wang X and Chen Y 2016 *Opt. Express* **24** 15059

[22] Chen Y H, Ye X L, Wang J Z, Wang Z G and Yang Z 2002 *Phys. Rev. B* **66** 195321

[23] Aspnes D E 1985 *Journal of Vacuum Science & Technology B* **3** 1498

[24] Chen Y H, Ye X L, Xu B, Wang Z G and Yang Z 2006 *Appl. Phys. Lett.* **89** 051903

[25] Tang C G, Chen Y H, Xu B, Ye X L and Wang Z G 2009 *J. Appl. Phys.* **105** 103108

[26] Zhang WF, Qin Z Y and Yang Z 2005 *J. Appl. Phys.* **97** 074314

[27] Lastras-Martinez L F, del Pozo-Zamudio O, Herrera-Jasso R, Ulloa-Castillo N A, Balderas-Navarro R E, Ortega Gallegos J and Lastras-Martinez A 2012 *Physica Status Solidi B-Basic Solid State Physics* **249** 1119

[28] Lastras-Martinez L F, Castro-Garcia R, Balderas-Navarro R E and Lastras-Martinez A 2009 *Appl. Opt.* **48** 5713

[29] Gao H S, Liu Y, Zhang H Y, Wu S J, Jiang C Y, Yu J L, Zhu L P, Li Y, Huang W and Chen Y H 2014 *Appl. Phys. Lett.* **104** 053106

[30] Lu L, Gao Z Y, Shen B, Xu F J, Huang S, Miao Z L, Hao Y, Yang Z J, Zhang G Y, Zhang X P, Xu J and Yu D P 2008 *J. Appl. Phys.* **104** 123525

[31] Lu L, Gao Z Y, Shen B, Xu F J, Huang S, Miao Z L, Hao Y, Yang Z J, Zhang G Y, Zhang X P, Xu J and Yu D P 2008 *J. Appl. Phys.* **104** 123525

[32] Ge C Z, Hsu C C and Ming N B 1994 *J. Cryst. Growth* **142** 133

[33] Shin Y J, Kim W J, Kim H Y and Bahng W 2013 *Dislocation analysis of 4H-and 6H-SiC single crystals using micro-Raman spectroscopy* (Materials Science Forum vol. 740-742) pp. 481–484

[34] Matsuoka D, Yamamoto H, Nishino S, Hasuike N, Kisoda K and Harima H 2009 *Raman Scattering Study of Stress Distribution around Dislocation in SiC* (Materials Science Forum vol. 600-603) pp. 337–340

[35] Gmeinwieser N and Schwarz U T 2007 *Phys. Rev. B* **75** 245213